International Journal of Multiphase Flow 35 (2009) 725–737

Contents lists available at ScienceDirect

International Journal of Multiphase Flow

journal homepage: www.elsevier.com/locate/ijmulflow

Near-critical CO_2 liquid–vapor flow in a sub-microchannel. Part I: Mean-field free-energy D2Q9 lattice Boltzmann method

Shi-Ming Li [1], Danesh K. Tafti *

Mechanical Engineering Department, Virginia Polytechnic Institute and State University, Virginia Tech, Blacksburg, VA 24061, USA

ARTICLE INFO

Article history:
Received 3 November 2008
Received in revised form 6 April 2009
Accepted 6 April 2009
Available online 11 April 2009

Keywords:
Lattice Boltzmann method
Fluid–wall boundary condition
Liquid–vapor interfacial flow
Moving contact line

ABSTRACT

The mean-field free-energy based lattice Boltzmann method (LBM) is developed for the calculation of liquid–vapor flows in channels. We show that the extensively used common bounceback boundary condition leads to an unphysical velocity at the wall in the presence of surface forces that arise from any local forces such as gravity, fluid–fluid and fluid–solid interactions. We then develop a mass-conserving velocity-boundary condition which eliminates the unphysical velocities. An important aspect of the overall LBM model is the inclusion of the correct physics to simulate different wall wettabilities and dynamic contact lines. The model is applied to static and dynamic liquid–vapor interfacial flows and compared to theory. The model shows good agreement with three well established theories of contact line dynamics.

1. Introduction

The characterization of immiscible liquid–vapor interfaces at solid surfaces is important in a wide range of fundamental topics ranging from boiling, condensation, transport of liquid–vapor mixtures in microchannels, electrowetting, with applications in power generation, refrigeration/air-conditioning, optoelectronics, and in biotechnology. Under static conditions, molecular attraction between solid–liquid–vapor phases results in a three-phase contact line which is adequately described by Young's law relating the equilibrium contact angle to the intermolecular forces or the surface tension forces between the three phases. Under dynamic condition, on the other hand, the contact line moves resulting in advancing and receding contact angles, which are not known *a priori*. Molecular dynamics (MD) simulations have been used successfully to resolve many details of moving contact lines at the molecular scales, such as the work by Allen and Tildesley (1987), De Ruijter et al. (1999), Barrat and Bocquet (1999) and Qian et al. (2003, 2004). However, MD is limited to nanoscales and computationally demanding even for fundamental research problems. Continuum methods, on the other hand, have the potential to describe moving contact lines on macroscopic length- and time-scales. However, classical discontinuous interface methods (e.g. Hirt and Nichols, 1981; Unverdi and Tryggvason, 1992a,b; Osher and Sethian, 1988; Sethian 1996) with a no-slip boundary condition lead to a stress-singularity at the moving contact line (Dussan, 1979; De Gennes, 1985). To resolve the singularity, the no-slip boundary condition has to be relaxed to a slip boundary treatment in the framework of the Navier–Stokes equations through an empirical relation between the contact angle and the slipping velocity (Shkhmurzaev, 1997; Oron et al., 1997), limiting the predictive capability of discontinuous methods.

Unlike discontinuous interface methods, diffuse interface methods (Antanovskii, 1995; Jasnow and Vinals; 1996; Anderson et al., 1998; Jacqmin, 1999, 2000; Jamet et al., 2001) are based on the explicit recognition that phase interfaces undergo a rapid but smooth transition of the physical quantities of the bulk phases, making the interfaces directly resolvable, at least in theory, in a numerical calculation. While all the discontinuous interface methods have their foundations in hydrodynamics, liquid–vapor systems, on the other hand, require a thermodynamic basis to facilitate evaporation and condensation between the two phases. The diffuse interface methods, which are based on the mean-field representation of the free-energy of the fluid, provide a thermodynamically consistent and numerically simple framework to deal with liquid–vapor phase transitions (condensation and evaporation), interface capillarity, and hydrodynamics. In addition, complex topological changes in the liquid–vapor interface can be accommodated with much greater ease within the framework of the diffuse interface method.

A number of two-phase diffuse interface methods have been developed under the umbrella of lattice Boltzmann methods (LBMs) (Gunstensen et al., 1991; Shan and Chen, 1993, 1994; Swift et al. 1995, 1996; He et al., 1998, He and Doolen, 2002; Luo, 1998; Zhang et al., 2004; Li and Tafti, 2007). LBM, which has its origins in lattice-gas cellular automata and can also be derived from the continuous Boltzmann equation, operates in the mesoscopic regime on

* Corresponding author. Tel.: +1 540 231 9975; fax: +1 540 231 9100.
E-mail addresses: shiming.li@ge.com (S.-M. Li), dtafti@vt.edu (D.K. Tafti).
[1] Present address: 273-234, 1 River Road, Schenectady, NY 12345, USA.

0301-9322/$ - see front matter © 2009 Elsevier Ltd. All rights reserved.
doi:10.1016/j.ijmultiphaseflow.2009.04.001

particle distribution functions on a lattice. Hence for engineering applications it is a good compromise between continuum simulations at the macro-scales, where much of the micro-physics is averaged out, and molecular dynamics calculations which are limited to process length and time scales at most in the nanometer and nanosecond range, respectively.

Central to many of the LBM methods for calculating two-phase flows, however, is the use of the nonlocal pressure equation based on the square-gradient theory (Swift et al., 1995, 1996; He et al., 1998; He and Doolen, 2002). In the square-gradient theory, the free-energy density of fluid is represented by two components, one pertaining to the homogeneous energy density of the bulk fluid phases from classical equilibrium thermodynamics and the second due to the inhomogeneous or molecular attractive forces between dissimilar phases, which is represented by the square of the gradient of fluid density following van der Waals (Rowlinson, 1979) and Cahn and Hilliard (1958). The nonlocal pressure equation of the square-gradient theory (Rowlinson, 1979; Swift et al., 1995; He and Doolen, 2002) thus includes the square of fluid density gradient term.

It is recognized that the square-gradient theory poses some limitations on the description of phase interfaces near a solid wall (Sullivan, 1981; Van Giessen et al., 1997; Zhang et al., 2004). In micorchannels and sub-microchannels, the solid walls or the wettabilities of the solid walls are a critical factor in determining the interfacial flows. When a solid boundary exists, the impenetrable solid wall imposes a discontinuity on the fluid density near the wall. In practical implementation, it is not easy to obtain realistic contact angles and fluid density distributions near a wall based on the square-gradient theory. Briant et al. (2002, 2004) have applied the square-gradient theory based LBM and studied the moving contact line dynamics. During their simulation, they fixed the contact angle *a priori* and do not allow it to change based on the flow dynamics. On the other hand, different investigations (Zhang et al., 2004; Li and Tafti, 2006) have shown that this limitation of the square-gradient theory can be overcome with an integral representation of the free-energy.

The objective of the two part paper is to investigate the evolution of flow interfaces or flow regimes encountered in a sub-microchannel for near-critical CO_2 as the working fluid. In this paper we incorporate the more general and consistent integral expression of the nonlocal pressure of liquid–vapor interfacial flows developed in Li and Tafti (2007) into D2Q9 LBM. In addition, we show that in the presence of surface forces, the commonly used bounceback boundary condition leads to significant unphysical velocities at walls. To overcome this shortcoming, we develop a consistent mass conserving velocity-boundary condition for the D2Q9 lattice configuration in the presence of surface forces. The numerical results presented in this paper establish that the D2Q9 LBM with the new boundary condition has the capability to successfully simulate static and dynamic liquid–vapor interfaces and contact line dynamics with different wall wettabilities.

2. Mean-field free-energy D2Q9 LBM

For completeness, first, we briefly summarize the integral expression of the nonlocal pressure equation developed for liquid–vapor interfacial flows (Li and Tafti, 2007). This nonlocal pressure equation is based on a more general expression of the total Helmholtz free-energy for liquid–vapor interfacial flows in the framework of the mean-field theory (van Kampen, 1964; Sullivan, 1981; Rowlinson and Widow, 1982) as follows:

$$H = \int_\Omega \psi[n(\mathbf{r})]\, d^3\mathbf{r} + \frac{1}{4}\int\int_\Omega w(\mathbf{r},\mathbf{r}')[n(\mathbf{r}') - n(\mathbf{r})]^2\, d^3\mathbf{r}\, d^3\mathbf{r}' \tag{1}$$

In the above equation, H is the total Helmholtz free-energy of the whole liquid–vapor system; $\psi(n)$ is the local free-energy density; n is the local fluid density; and Ω represents the volume of the whole liquid–vapor system. $\mathbf{r}$ and $\mathbf{r}'$ in the equation are two spatial location vectors. The first term on the right-hand side of the above equation represents the free-energy due to the homogeneous energy density of the bulk fluid phases from classical equilibrium thermodynamics. The second term is the mean-field representation of the free-energy due to the attraction between molecules accounting for inhomogeneities of fluid density at liquid–vapor interfaces. The interparticle pairwise attraction potential $-w(\mathbf{r},\mathbf{r}')$ is everywhere non-positive. For a homogeneous system, the second term reduces to zero and Eq. (1) equates the free-energy derived from equilibrium thermodynamics.

Based on the free-energy expression of Eq. (1), the nonlocal pressure equation for liquid–vapor interfacial flow is obtained by Li and Tafti (2007) as

$$p[n(\mathbf{r})] = n\psi' - \psi - n\int_\Omega w(\mathbf{r},\mathbf{r}')[n(\mathbf{r}') - n(\mathbf{r})]\, d^3\mathbf{r}' - \frac{1}{4}\int_\Omega w(\mathbf{r},\mathbf{r}')[n(\mathbf{r}') - n(\mathbf{r}')]^2\, d^3\mathbf{r}' \tag{2}$$

where ψ' is the derivative of the local free-energy density ψ to the local fluid density n. For a homogeneous fluid system, the last two terms reduce to zero and Eq. (2) equates the pressure equation of equilibrium thermodynamics.

Under the assumption of slow density variations across the liquid–vapor interface, Li and Tafti (2007) have shown that the nonlocal pressure equation expressed by Eq. (2) reduces to, and is consistent with the nonlocal pressure equation of the square-gradient theory used in many LBM methods for calculating two-phase flows (Swift et al., 1995, 1996; He et al., 1998; He and Doolen, 2002). Therefore, Eq. (2) is a more general expression of the nonlocal pressure equation. As mentioned earlier in this paper, the integral form of the nonlocal pressure equation eliminates the limitations of the square-gradient theory on the description of phase interfaces near a solid wall.

To incorporate the nonlocal pressure into D2Q9 LBM, we start with the D2Q9 lattice Boltzmann BGK equation (Chen et al., 1991; Qian et al., 1992):

$$f_i(\mathbf{x}+\mathbf{e}_i, t+1) - f_i(\mathbf{x},t) = \frac{1}{\tau}[f_i^{\mathrm{eq}}(\mathbf{x},t) - f_i(\mathbf{x},t)], \quad i = 0,1,2,\ldots,8 \tag{3}$$

where t and τ are the time step and the relaxation time of particle collision. $\mathbf{x}$ and $\mathbf{e}_i$ represent the lattice site location vector and the direction vector in i_{th} lattice link, respectively. $f_i(\mathbf{x},t)$ is the particle distribution function and $f_i^{\mathrm{eq}}(\mathbf{x},t)$ is the equilibrium particle distribution.

D2Q9 lattice configuration is shown in Fig. 1. The nine vectors of the lattice links are documented as follows:

$$\mathbf{e}_0 = [0,0] \tag{4}$$

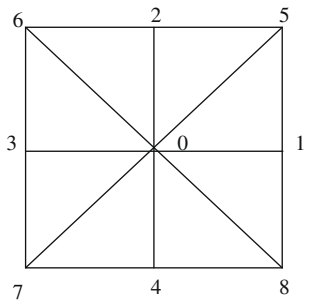

Fig. 1. D2Q9 lattice configuration.

$$\mathbf{e}_i = \frac{\Delta r}{\Delta t}\left[\cos\frac{\pi}{2}(i-1), \sin\frac{\pi}{2}(i-1)\right], \quad i = 1,2,3,4 \tag{5}$$

$$\mathbf{e}_i = \frac{\Delta r}{\Delta t}\sqrt{2}\left[\cos\left[\frac{\pi}{2}(i-1)+\frac{\pi}{4}\right], \sin\left[\frac{\pi}{2}(i-1)+\frac{\pi}{4}\right]\right], \quad i = 5,6,7,8 \tag{6}$$

where both Δr and Δt are the lattice length and time step, respectively. The sound speed of the D2Q9 lattice model c_s is

$$c_s^2 = \frac{1}{3}c^2 = \frac{1}{3}\left(\frac{\Delta r}{\Delta t}\right)^2 = R_g T \tag{7}$$

where R_g is the gas constant; c is the lattice fluid particle velocity; and T is the temperature.

The equilibrium particle distribution is given by Qian et al. (1992) and Chen et al. (1992) as

$$f_i^{eq} = w_i n\left[1 + 3\mathbf{e}_i\cdot\mathbf{u} + \frac{9}{2}(\mathbf{e}_i\cdot\mathbf{u})^2 - \frac{1}{2}\mathbf{u}\cdot\mathbf{u}\right], \quad i = 0,1,2,\ldots,8 \tag{8}$$

where $\mathbf{u}$ is the equilibrium velocity and w_i ($i = 0, 1, \ldots, 8$) are the weighting factors accounting for the variation of different lengths of the lattice links. The weighting factors have the following values to recover the Navier–Stokes equations:

$$w_0 = \frac{4}{9} \tag{9}$$

$$w_i = \frac{1}{9}, \quad i = 1,2,3,4 \tag{10}$$

$$w_i = \frac{1}{36}, \quad i = 5,6,7,8 \tag{11}$$

From the above definition, following the standard Chapman–Enskog procedure, the Navier–Stokes-like equations for a liquid–vapor system are recovered, having the fluid density n, velocity $\mathbf{v}$, and viscosity as follows:

$$n = \sum_{i=0}^{8} f_i \tag{12}$$

$$n\mathbf{v} = \sum_{i=1}^{8} f_i\mathbf{e}_i + \frac{1}{2}\mathbf{F} \tag{13}$$

$$\nu = \frac{\Delta r^2}{3\Delta t}(\tau - 0.5) \tag{14}$$

The nonlocal pressure expressed by Eq. (2) is incorporated into D2Q9 LBM through a fluid–fluid force term $\mathbf{F}_{ff}$ defined as follows (Zhang et al., 2004):

$$\mathbf{F}_{ff} = -\nabla\{p[n(\mathbf{r})] - c_s^2 n(\mathbf{r})\} \tag{15}$$

In general, the force $\mathbf{F}$ on a fluid particle in multiphase flow includes

$$\mathbf{F} = \mathbf{F}_{ff} + \mathbf{F}_{sf} + \mathbf{F}_o \tag{16}$$

where $\mathbf{F}_{sf}$ is solid–fluid attraction and $\mathbf{F}_o$ represents other possible external forces such as gravity and electrical forces. The total force $\mathbf{F}$ is then incorporated into the LBM through the equilibrium velocity $\mathbf{u}$ (Shan and Chen, 1993, 1994) as:

$$n\mathbf{u} = \sum_{i=1}^{8} f_i\mathbf{e}_i + \tau\mathbf{F} \tag{17}$$

Eqs. (2)–(17) complete the definition of the mean-field free-energy D2Q9 LBM for liquid–vapor interfaces.

2.1. Numerical implementation

To implement the LBM numerically, a representation of the local free-energy density $\psi(n)$ is needed. The expression of free-energy in mean-field theory given by van Kampen (1964) is used for this purpose,

$$\psi(n) = nk_bT\ln\frac{n}{1-bn} - an^2 - nk_bT \tag{18}$$

where a and b are the van der Waals constants, which are specified as $a = 9/49$ and $b = 2/21$ in the Part I of this paper, and k_b is the Boltzmann constant. Eq. (18) leads to the well-known van der Waals equation of state:

$$p_0 = n\psi' - \psi = \frac{nk_bT}{1-bn} - an^2 \tag{19}$$

where p_0 is the bulk phase pressure.

The interparticle attraction potential $-w(\mathbf{r}, \mathbf{r}')$ for D2Q9, similar to the treatment for D2Q7 as documented in Li and Tafti (2007), is approximated as

$$-w(\mathbf{r},\mathbf{r}') = \begin{cases} -K, & |\mathbf{x}'-\mathbf{x}'| = \Delta r \\ -K_f K, & |\mathbf{x}'-\mathbf{x}| = \sqrt{2}\Delta r \\ 0, & |\mathbf{x}'-\mathbf{x}| = \text{others} \end{cases} \tag{20}$$

where $-K$ is the constant representing the effective fluid–fluid attraction potential when the distance from one fluid particle to another is at the unit lattice length $|\mathbf{x}' - \mathbf{x}'| = \Delta r$. $\mathbf{x}$ and $\mathbf{x}'$ represent the different lattice site location vectors. K_f is the decay factor of the attraction potential when the interaction distance changes from Δr to $\sqrt{2}\Delta r$. Like the simulations with D2Q7 by Li and Tafti (2007), we use $K = 0.01$ for all the simulations in the Part I of this paper.

The solid–fluid attraction force $\mathbf{F}_{sf}$ is simulated in a manner consistent with the fluid–fluid interaction. The wall is considered as a solid phase with the constant density n_s and the attraction for each solid–fluid pair of particles is then similarly expressed as:

$$\mathbf{F}_{sf}(\mathbf{x}_s,\mathbf{x}_f) = \begin{cases} -Kn_s(\mathbf{x}_s)n(\mathbf{x}_f)(\mathbf{x}_f-\mathbf{x}_s), & |\mathbf{x}'-\mathbf{x}| = \Delta r \\ -KK_f n_s(\mathbf{x}_s)n(\mathbf{x}_f)(\mathbf{x}_f-\mathbf{x}_s), & |\mathbf{x}'-\mathbf{x}| = \sqrt{2}\Delta r \\ 0, & |\mathbf{x}'-\mathbf{x}| = \text{others} \end{cases} \tag{21}$$

where $n_s(\boldsymbol{x}_s)$ is the density of the solid wall at the location $\mathbf{x}_s$.

Using the following expression:

$$K_W = Kn_s(\mathbf{x}_s), \tag{22}$$

Eq. (21) becomes

$$\mathbf{F}_{sf}(\mathbf{x}_s,\mathbf{x}_f) = \begin{cases} -K_W n(\mathbf{x}_f)(\mathbf{x}_f-\mathbf{x}_s), & |\mathbf{x}'-\mathbf{x}| = \Delta r \\ -K_f K_W n(\mathbf{x}_f)(\mathbf{x}_f-\mathbf{x}_s), & |\mathbf{x}'-\mathbf{x}| = \sqrt{2}\Delta r \\ 0, & |\mathbf{x}'-\mathbf{x}| = \text{others} \end{cases} \tag{23}$$

Thus, Eq. (23) includes only one constant K_W, which represents the specific properties of a solid wall in the interaction with the fluid on its surface, the strength of molecular solid–fluid attraction or the wettability.

3. Velocity-boundary condition with external force

In this section, we first show that an unphysical velocity exists with the widely used bounceback boundary treatment when a surface force is present. To clearly describe the problem, we examine the dynamics of fluid particles inside a domain (away from the boundary). In the LBM procedure, Eq. (17) displays that an external force $\mathbf{F}$ is incorporated into the LBM through the equilibrium velocity $\mathbf{u}$. In general, a lattice Boltzmann equation represents the streaming and collision processes of fluid particles, as shown by Eq. (3). In the current LBM, $\mathbf{F}$ does not explicitly act on fluid particles during the streaming and collision processes. Instead, it acts through the equilibrium distribution functions $f_i^{eq}(\mathbf{x}, t)$ as defined in Eq. (8). On a boundary of the domain, on the other hand, the

fluid particle convection and collision processes are not simulated through the lattice Boltzmann equation (Eq. (3)) and $f_i^{eq}(\mathbf{x},t)$. Instead, the common bounceback boundary condition is extensively used to deal with wall boundaries. Mathematically, the common bounceback boundary condition gives a zero sum of the following vectors:

$$\sum_{i=1}^{8} f_i \mathbf{e}_i = 0 \tag{24}$$

We can see that satisfying Eq. (24) through the bounceback condition does not yield zero velocity or a no-slip condition on a wall in the presence of surfaces force **F** as shown by Eq. (13). The bounceback condition applied to Eq. (13) leaves behind a generally non-zero unphysical velocity $\mathbf{F}/2n$. As shown in Eq. (16), the force **F** includes fluid–fluid attraction $\mathbf{F}_{ff}$, solid–fluid attraction $\mathbf{F}_{sf}$, and other possible external forces $\mathbf{F}_o$ such as gravity and electrical forces. At a solid boundary node, in addition to fluid–fluid attraction, there is a solid–fluid attraction, which represents the wettability of the solid wall. Both of these forces are non-zero. The magnitude of this unphysical velocity due to the wettability can be estimated by applying Eq. (23), resulting in an unphysical velocity of $K_W/2$. It will be shown later in this paper that K_W can be any value from 0.0 to 0.010 or even larger to express the complete wetting range from non-wetting to a completely wetting wall. Therefore, the magnitude of the unphysical velocity could be as large as that equivalent to the Mach number $Ma \sim 0.1$. This is not a trivial velocity in incompressible, microchannel flow, especially for many engineering applications where many solid surfaces are highly wetting surfaces, that is, K_W usually takes on large values.

It is noted that this unphysical velocity due to the bounceback boundary condition is not caused by the choice of the implementation method of the external force term, **F** into the LBM. In the literature, there are three common ways to incorporate a force term into LBM. One is the same as the current LBM, through Eq. (13). Another method is adding a force term directly to the lattice Boltzmann equation. The third method is a combination of the above two, including the force term in the lattice Boltzmann equation plus defining an equilibrium velocity similar to Eq. (13). We have shown that all three approaches produce a similar unphysical velocity on the wall in the presence of a surface force. Hence the following development has a broad range of applicability. It is noted that the unphysical velocity discussed above due to the common bounceback boundary condition is different from the "slip velocity" of bounceback boundary treatments discussed frequently in the literature, such as Lee and Lin (2005). The unphysical velocity found in the current paper is only related to the existence of external forces and does not change with the relaxation time of the LBM. When no external force is present, such as a single phase flow of an ideal fluid without gravity and no wettability as well as fluid–fluid attraction considered, the unphysical velocity disappears.

The idea of Zou and He (1997) is applied here to solve the problem of the above unphysical velocity on the solid boundary. For single phase flow, Zou and He (1997) have proposed a velocity–pressure boundary condition. Their idea is to solve a system of equations consisting of the unknown particle distribution functions on the boundary in conjunction with a bounceback condition for a partially unknown particle distribution function(s). For the non-slip boundary condition of a static wall or a moving solid boundary, the flow velocity on the wall is known and imposed on the solid boundary. When the fluid velocity is unknown on a boundary, such as an inlet or outlet of a channel, the pressure (which is equivalent to density in single phase flow) can be specified on the boundary as a replacement. In the development of the velocity–pressure boundary condition, Zou and He (1997) did not consider situations in which an external force is present at the boundary.

According to our theoretical development process, we describe the new boundary condition in two layers. The first layer is an application of Zou and He's idea to a boundary with surface force to eliminate the unphysical velocity. The second layer is a further improvement over the first layer. Fig. 2 shows the D2Q9 lattice aligned with a bottom wall. For the lattice site "P" on the bottom wall, there are nine particle distribution functions, f_0, f_1, f_2, f_3, f_4, f_5, f_6, f_7, and f_8, the same as that inside the domain. Among the nine, f_0, f_1, f_3, f_4, f_7, and f_8 are known after a streaming step, while the rest, f_2, f_5, and f_6 come from outside the domain and therefore are unknown and need to be defined.

Eq. (13), which includes the external force term, gives

$$f_5 - f_6 = nV_x - f_1 + f_3 + f_7 - f_8 - F_x/2 \tag{25}$$
$$f_5 + f_6 = nV_y - f_2 + f_4 + f_7 + f_8 - F_y/2 \tag{26}$$

where V_x and V_y are two components of the velocity vector **V**, that is $V_x i_x + V_y i_y = \mathbf{V}$.

Because we have three unknowns f_2, f_5, and f_6; we need another equation together with the above two to close the problem. In the velocity–pressure boundary condition, Zou and He (1997) further assume that the *non-equilibrium* part of the particle distribution function in the wall normal direction, f_2 satisfies the bounceback condition. In the present study, we could use the same non-equilibrium bounceback condition to close the equation system. However, our numerical tests have shown that letting f_2 itself satisfy the bounceback condition generates the equivalent results. Because the bounceback condition of f_2 itself is simpler, this treatment is used to replace the non-equilibrium bounceback condition.

With f_2 defined and the velocity **V** specified on the solid wall (**V** = 0 for a static solid wall, for example), Eqs. (25) and (26) yield

$$f_5 = (nV_x + nV_y - f_1 - f_2 + f_3 + f_4 + 2f_7 - F_x/2 - F_y/2)/2 \tag{27}$$
$$f_6 = (-nV_x + nV_y + f_1 - f_2 - f_3 + f_4 + 2f_8 + F_x/2 - F_y/2)/2 \tag{28}$$

The fluid density n on the boundary is then obtained through Eq. (12) as:

$$n = f_0 + f_1 + f_2 + f_3 + f_4 + f_5 + f_6 + f_7 + f_8 + f_9 \tag{29}$$

Eqs. (27)–(29) together with the bounceback condition for f_2 complete the definition of the boundary condition for D2Q9, which resolves the issue of the unphysical velocity on the wall when a surface force is present. For a static solid wall, the non-slip boundary condition can be implemented directly from the three Eqs. (27)–(29). For a moving wall, on the other hand, the unknown density n on the wall is coupled in the equations and thus the boundary condition is implemented through solving the three coupled equations. It is further noted that with the new boundary condition, the equilibrium distribution functions $f_i^{eq}(\mathbf{x},t)$ and the collision process defined by the lattice Boltzmann equation are applied equally to both internal and boundary nodes.

In our numerical simulations, the above developed boundary condition gives good results in simulating static liquid–vapor

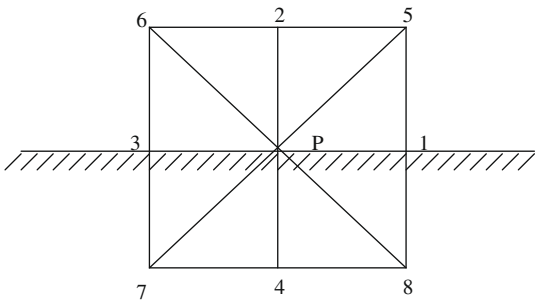

Fig. 2. D2Q9 lattice configuration on a solid wall.

interfaces. However, our numerical results (presented later) reveal that there is a net mass flux across the solid wall, especially near a contact line for solid–liquid–vapor interfaces. These errors result from the non mass conservation at each instant even though a zero velocity on the solid wall is realized on a time-average level during the combined particle streaming and collision process. For clarity, we call the above developed boundary condition as BC1 while the following improved boundary condition as BC2.

While BC1 guarantees zero relative velocity of fluid on the wall in the averaged sense or on the mesoscopic/macroscopic level, the following improvement of BC2 is to impose mass conservation on the microscopic level: At every time step in the LBM, the mass conservation is imposed on the microscopic levels of the fluid particle activities, collision and convection. In BC1, we invoke the assumption that f_0 does not change before and after the particle collision. In BC2, instead, we define f_0 after the collision step according to the mass conservation of all particle functions on each lattice site. During a full LBM time step, f_0, f_4, f_7, and f_8 leave the domain at the instant t^{+0}, while the fluid particles f_0, f_2, f_5, and f_6 enter the domain at the instant $(t+1)^{-0}$. The mass conservation at this lattice site requires:

$$f_0 = f_0^t + f_4^t + f_7^t + f_8^t - (f_2 + f_5 + f_6) \tag{30}$$

Thus, we have four equations (27)–(30) for the five unknowns $f_0, f_2\ f_5, f_6, n$. These four equations with the bounceback condition for f_2 define the mass-conserving velocity-boundary condition.

For a moving solid wall, the unknown functions f_0, f_5, f_6, n are obtained by solving Eqs. (27)–(30). For a static solid wall, on the other hand, f_5 and f_6 are first obtained by Eqs. (27) and (28). f_0 is then obtained by substitution of f_2, f_5, and f_6 into Eq. (30). The fluid density n on the wall is then calculated through Eq. (29).

For other walls of a flow domain, such as top wall, left and right side wall, the mass conservation velocity-boundary condition can be implemented in a similar way to that for the bottom wall.

4. Numerical results and verifications

We use Laplace law of capillarity to test the capability of the D2Q9 LBM model in simulating static liquid–vapor interfaces. We simulate droplets on a wall with different wettabilities to verify the capability in simulating different static contact angles. In addition, we use capillary waves and moving contact lines to verify the capability of the D2Q9 LBM model for simulating dynamic interfaces for both liquid–vapor interfaces and solid–liquid–vapor interfaces.

4.1. Laplace law of capillarity

For a droplet in vapor, the 2D Laplace's law of capillarity states:

$$P_{\text{in}} - P_{\text{out}} = \frac{\gamma}{R} \tag{31}$$

where P_{in} and P_{out} are the fluid pressures inside and outside the droplet; γ is the surface tension and R is the radius of the droplet.

With D2Q7 LBM, we have used Laplace law to verify the mean-field free-energy nonlocal pressure equation and its LBM (Li and Tafti, 2007). In the present context, consequently, our focus is on examining the difference between D2Q9 and D2Q7, that is, the change of the interparticle potential with different spaced lattice sites, as expressed by the decay factor K_f in the potential in Eq. (20). In the literature, different researchers use different values for the decay factor K_f. Most of them take K_f to be either 1/2 or 1/4. In fact, fluid–fluid interaction of many fluids can be well approximated by the well-known Lennard-Jones potential, which is:

$$w_{L\text{-}J}(\mathbf{r}' - \mathbf{r}) = 4\varepsilon\left[\left(\frac{\sigma}{\mathbf{r}' - \mathbf{r}}\right)^{12} - \left(\frac{\sigma}{\mathbf{r}' - \mathbf{r}}\right)^{6}\right] \tag{32}$$

where ε and σ are physical constants, which are chosen to some specific values according to the fluids simulated. The first term of the right-hand side in the above equation is the repulsive potential, while the second term is the attraction potential. According to Lennard-Jones potential, $K_f = 1/8$ appears appropriate when the lattice distance changes from Δr to $\sqrt{2}\Delta r$. This result is different from what is generally used in the literature.

To find an appropriate value of the decay factor K_f for the current LBM, we perform numerical simulations with $K_f = 1/2$, 1/4, 1/8, and 1/16, respectively. The temperature of the liquid–vapor system in the simulations is $k_bT = 0.55$. A periodic boundary condition is applied on the four sides of the simulation domain. For the present purpose, we simulate the domain with the dimension of 128×128, using the relaxation time $\tau = 1$. Our simulations start with a rectangular block of liquid located in the middle of the domain with the saturated vapor distributed everywhere else over the domain. As the calculation proceeds, the droplet evolves from its initial rectangular shape to a circular shape at around 1500 iterations. Beyond the time step 1500, the shape of the droplet changes little, similar to the results of D2Q7 LBM (Li and Tafti, 2007). This indicates that the convergence speed of D2Q9 is about the same as that of D2Q7. The spurious residual velocity of the current simulations, however, attains the order 10^{-9} at the time step 10,000 over the whole simulation domain, which is three orders of magnitude lower than that of D2Q7.

Fig. 3 shows the pressure differences inside and outside of the droplets with different droplet sizes simulated to the time step 10,000. The figure also displays the results with the four different values of K_f. In the figure, the solid circles, triangles, squares, and hollow circles represent the results with $K_f = 1/2$, 1/4, 1/8, and 1/16, respectively. The four solid lines are the linear correlations of the respective LBM results for the different K_f factors. The results show that the pressure difference across the droplet increases linearly with the decrease of the droplet radius for all four K_f factors, indicating that the LBM simulations with the different factors all represent the linear characteristic of the Laplace law very well.

According to the Laplace law, the slope of the correlation line in Fig. 3 gives the surface tension of the liquid–vapor system, which yield $\gamma = 0.00760$, 0.00825, 0.00860, and 0.00880 for $K_f = 1/2$, 1/4, 1/8, and 1/16, respectively. The exact solution of the surface tension based on the mean-field theory gives $\gamma = \text{const}\cdot\theta^{\beta}$ (Van Giessen et al., 1998), where γ is the surface tension of a planar interface; θ is a normalized temperature, $\theta = (T_c - T)/T_c$; T_c represents the critical temperature; the analytical mean-field theory gives $\beta = 3/2$. For the LBM fluid at $k_bT = 0.55$, the surface tension is 0.00824 (Li and Tafti, 2007), which is very close to the result with $K_f = 1/4$. Hence, the surface tension of the present simulations with $K_f = 1/4$ is consistent with the analytical solution of mean-field theory,

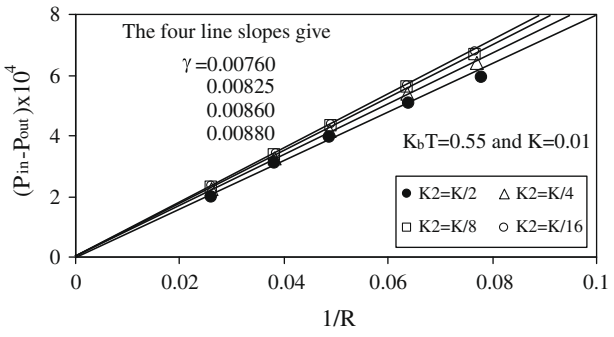

Fig. 3. Pressure difference between inside and outside of droplets for different droplet sizes, $k_bT = 0.55$, $K = 0.01$; four different symbols are the results for different K_f factors; four solid lines are the linear correlations of the results for the four different K_f factors.

and in all later simulations with D2Q9, therefore, we use the constant $K_f = 1/4$.

4.2. Capillary waves

Capillary waves are used to validate the D2Q9 LBM in simulating the dynamic characteristics of liquid–vapor interfaces without a solid wall. According to the theory of capillary waves (Lamb, 1945 and Landau and Lifshitz, 1987), the dispersion relation between the wave frequency ω and wave number k is given by:

$$\omega^2 \sim k^3 \tag{33}$$

The simulations are conducted at the temperature $k_bT = 0.53$ on a rectangular domain. Both the left and right sides of the domain are treated with periodic boundary conditions while a non-slip, solid boundary condition is imposed on the top and bottom walls. The simulations start with the initial conditions of zero velocity with the saturated liquid and vapor distributed in the lower and upper half of the domain, respectively. The LBM iterations are performed until an equilibrium planar interface is formed and the density profile across the interface shows little change. At this time, a single-period sine wave is imposed on the planar interface and the evolution of the interface location is then recorded. The wave number of the simulated domain is determined by the width of the domain ℓ as

$$k = \frac{2\pi}{\ell} \tag{34}$$

Table 1
Simulation summary: domain height h, width ℓ, wave number k, period $\check{T}$, and frequency ω.

Case	1	2	3	4	5	6
ℓ	31	41	51	61	71	81
h	150	200	250	300	350	400
k	0.20268	0.15325	0.1232	0.103	0.0885	0.07757
$\check{T}$	180	300	440	480	600	880
ω	0.03491	0.02094	0.01428	0.01309	0.01047	0.00714

The present simulations include six different domains as summarized in Table 1. The dimensions of the domains are chosen by considering the following requirements: (a) the domain height h is much bigger than the wave length ℓ such that "shallow water" effects are negligible; (b) the wave length is much larger than the wave amplitude, such that it is consistent with the assumption of small amplitude wave theory; and (c) the wave amplitude is much larger than the interface thickness, such that the changes of wave amplitudes are clearly distinguishable.

The capillary waves are displayed according to the density contour line at the averaged fluid density. Fig. 4 displays the snapshots of capillary waves at several typical time steps of a complete wave period. The results are shown for case 1 listed in Table 1, where the domain width is $\ell = 31$ and the domain height is $h = 150$. The relative time step Δt shown in Fig. 4 is counted from the time step when the sine wave is just imposed on the planar interface. The figure includes the snapshots at the start ($\Delta t = 0$), the middle ($\Delta t = 90$), and the end ($\Delta t = 180$) of a complete wave period. The rest of the snapshots are intermediate wave profiles. The results indicate that the period of the capillary wave is $\check{T} = 180$, which has an uncertainty of ±9 time steps as the data is recorded at every 10 time steps in the simulations. Based on the wave period obtained, the wave frequency is then obtained as 0.03491. Table 1 includes the wave numbers and frequencies for all cases studied. Fig. 5 displays the LBM results shown in Table 1 in solid dots. The solid line in the figure is the linear correlation of the six LBM points, which yields the line slope as 1.524. The exact solution of the slope, as shown in Eq. (33) is 1.50 and the error between the simulations and the exact solution is less than 2%.

4.3. Droplets on walls with different wettabilities

This section examines the capability of the current LBM to resolve static droplets on solid walls with different wettabilities, from completely non-wetting to fully wetting. A domain with 100×200 units is simulated, with a periodic boundary condition applied to the two sides (left and right) of the domain. The non-slip boundary condition is imposed on the bottom solid wall while a symmetric boundary condition is used on the top of the domain.

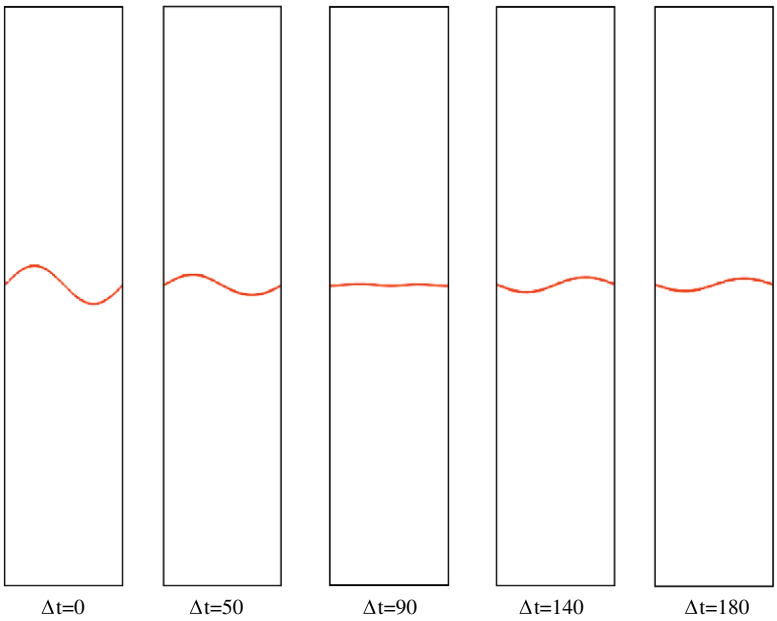

Fig. 4. Snapshots of capillary waves at different time steps, $k_bT = 0.53$, Case 1, $\ell = 31$, $h = 150$; the snapshots at the start ($\Delta t = 0$), the middle ($\Delta t = 90$), and the end of a complete wave period ($\Delta t = 180$). Additional two snapshots are the intermediate wave profiles.

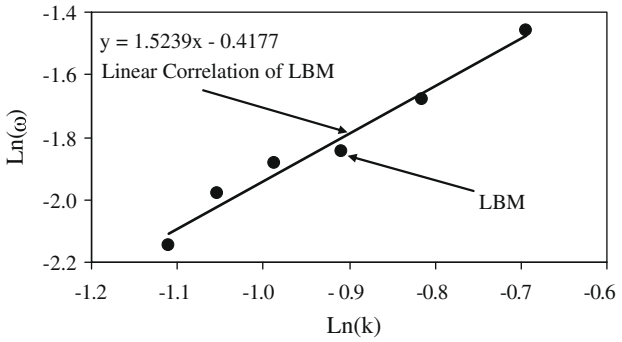

Fig. 5. Dispersion relation of capillary waves, $k_bT = 0.53$. Solid circle: the D2Q9 LBM; solid line: correlation for the LBM, which gives the line slope of 1.524; the exact solution gives the slope of 1.50.

Our simulations are performed at two temperatures, $k_bT = 0.51$ and 0.53 and with the relaxation time $\tau = 1$. The simulations start with the initial velocity of zero specified everywhere over the domain, with a small square block of liquid placed at the bottom of the domain with the rest of the domain specified as the saturated vapor. The liquid–vapor system attains the equilibrium states at around 6000 time steps after which the droplet shape and interface density profile change little. To obtain smaller spurious residual velocity, the iterations are continued to the time step 10,000, where the maximum spurious residual velocity is at the level of 10^{-7}–10^{-8} over the whole domain.

To compare the two new boundary conditions BC1 and BC2 proposed earlier, we simulate the problem with the two boundary conditions separately. Figs. 6 and 7 are the results with boundary condition BC1 applied on the bottom wall. Fig. 6 is the fluid density contour obtained at the time step 10,000, with $K_W = 0.04$, and at $k_bT = 0.53$. In the figure, the black and white colors represent the liquid and vapor density, respectively. The gray scales between the two represent the density change in the liquid–vapor interface. The figure displays the geometry of the liquid–vapor interface and the solid–liquid–vapor three-phase contact line (point in two-dimensions).

During the simulation, we recorded the mass flux across the non-penetrating solid wall at five different locations on the solid wall, at, near, and far away from the contact lines, as displayed in Fig. 7. It is shown that BC1 yields a net mass flux occurring across the solid wall, with different mass fluxes at different locations. The mass flux fluctuates with time, especially during the first 2000 time steps when the interface is moving toward a steady static state. Hence, in the case of moving dynamic interfaces, BC1 can result in significant errors everywhere on the solid boundary. The mass flux fluctuation decays to a certain level and then stays at this non-zero level during the rest of the simulation. At the locations away from the three-phase contact point, the steady level of the mass flux is close to zero, both on the liquid and vapor side. At the locations closer to the three-phase contact point, a slightly

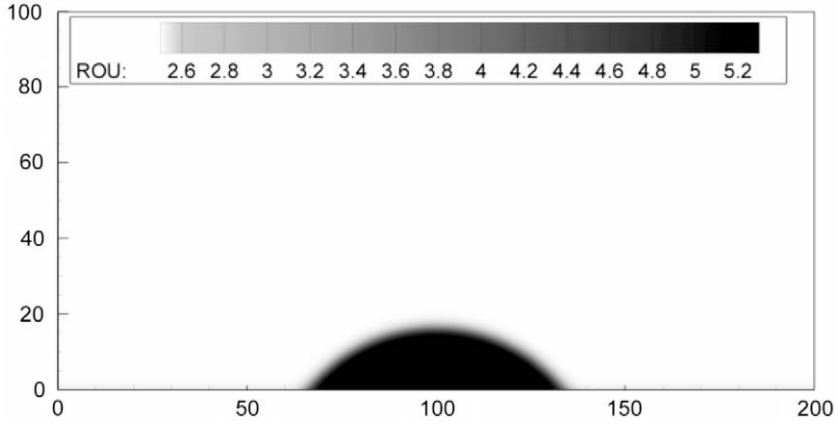

Fig. 6. Fluid density contour, $K_W = 0.04$, $k_bT = 0.53$.

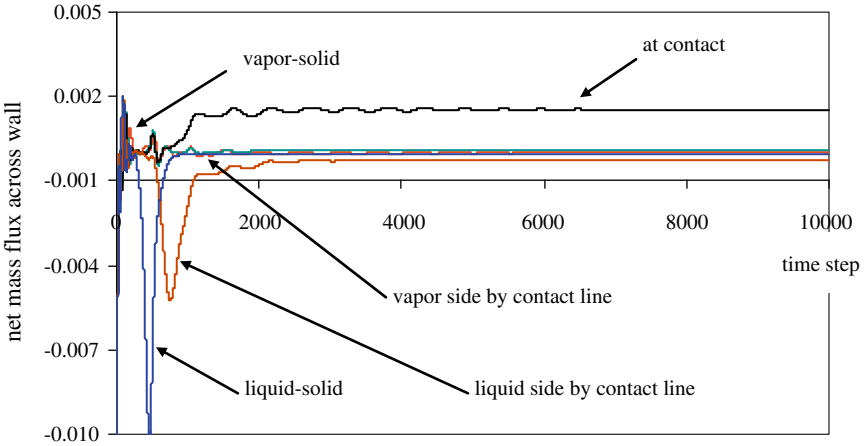

Fig. 7. Mass flux across solid wall at different locations $K_W = 0.04$, $k_bT = 0.53$.

higher level of the mass flux appears. However, right at the three-phase contact point, there is a much larger mass flux. Therefore, for static liquid–vapor interfaces BC1 gives fairly good results everywhere except at the location of the three-phase contact line.

When the mass conservation boundary condition BC2 is used, all mass fluxes on the solid wall are eliminated at every time step during our simulations: no net mass flux is recorded, both at the three-phase contact point and away from it. Fig. 8 shows a comparison of fluid density contour lines (plotted at the average density) with the two different boundary conditions. The results are obtained at the same condition with $K_W = 0.04$ at $k_bT = 0.53$. In Fig. 8, the thicker line is obtained with BC2 while the thinner line is the result with BC1. It is seen that at the equilibrium state, the difference of the droplet sizes with two boundary conditions is not significant at this wetting level, even though BC1 has the error at the three-phase contact line. Therefore, both BC1 and BC2 can give fairly good results for static liquid–vapor interfaces. However, the use of BC1 Does not guarantee the accurate simulation of moving contact lines. Hence, in the following simulations of moving contact lines we only apply the mass-conserving boundary condition (BC2) for solid walls.

Next, we test the capability of the current simulations to represent different wettabilities of solid walls. According to the well-known Young's law of wetting, different wettabilities of solid walls produce different contact angles at equilibrium. The Young's law of wetting governs the relation between fluid wettability and contact angle as:

$$\gamma \cos\theta_e = \gamma_{sv} - \gamma_{sl} \tag{35}$$

where θ_e is the equilibrium contact angle, and γ, γ_{sv}, and γ_{sl} are surface tension of liquid–vapor, solid-vapor, and solid–liquid, respectively. For a liquid–vapor system, γ is a constant at a given temperature, and γ_{sv} and γ_{sl} are determined by the molecular attraction between the solid wall and the liquid–vapor system. With our model, the surface tension is related with the parameter K_W, as shown in Eqs. (22) and (23). Thus, the capability of the LBM to simulate different wall wettabilities is examined with the relation between equilibrium contact angle θ_e and K_W from the simulation results.

Fig. 9 shows the fluid density contour lines of the simulated droplets on solid walls at $k_bT = 0.55$. The density contour lines are plotted at the average fluid density. Fig. 9 shows that different values of K_W produce different contact angles, as expected. When the strength of solid–fluid attraction is small, the droplet is completely detached from the wall due to the relatively stronger fluid–fluid attraction. As demonstrated in Fig. 9, the wall becomes dry at $K_W = 0.02$, with no liquid wetting the solid surface (it is noted that the droplet at $K_W = 0.02$ actually rests on the wall but due to the finite interface thickness, the average density contour is displaced from the wall). When K_W increases beyond 0.02, however, the droplet attaches to the wall. With a further increase in K_W, the contact angle decreases further. When K_W increases beyond 0.05, the droplet starts to wet the wall completely and a liquid film appears on the surface of the wall. These results show that the present D2Q9 model can represent the whole range of wettabilities, from a completely non-wetting (dry surface), through partially wetting, and finally to a complete wetting through variation of only the attraction strength K_W, which is in agreement with MD simulations (Barrat and Bocquet, 1999).

Fig. 10 displays more details of the relation between K_W and contact angle, where the solid circles are the LBM results and the line is a best linear fit of the LBM. This figure shows that the relationship between contact angle and K_W is close to linear, which agrees well with the independent studies by Yang et al. (2001) and Zhang et al. (2004). Figs. 11 and 12 are similar results at the different temperature, $k_bT = 0.53$. These results show that the current D2Q9 model has the capability to simulate different wettabilities very well.

4.4. Moving contact lines in a channel

4.4.1. Simulation procedure and outline

A vapor plug in a two-dimensional channel is studied to test the capability of the present D2Q9 model in simulating moving contact lines. Fig. 13 is the schematic of the simulation setup, where V is the interface velocity, θ_a and θ_r are advancing and receding contact angle, respectively. The relative magnitudes between capillary, vis-

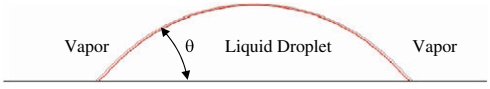

Fig. 8. Comparison of droplet on a wall with boundary conditions BC1 and mass conserving BC2, $K_W = 0.04$, $k_bT = 0.53$; the thicker line is obtained with the mass conservation boundary condition BC2; the thinner line is the results of the non-mass conservation boundary condition BC1.

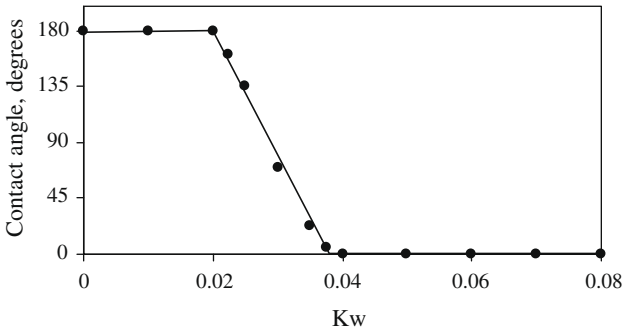

Fig. 10. Relation between contact angle and K_W, $k_bT = 0.55$; solid points are LBM simulations and solid line is their linear correlation.

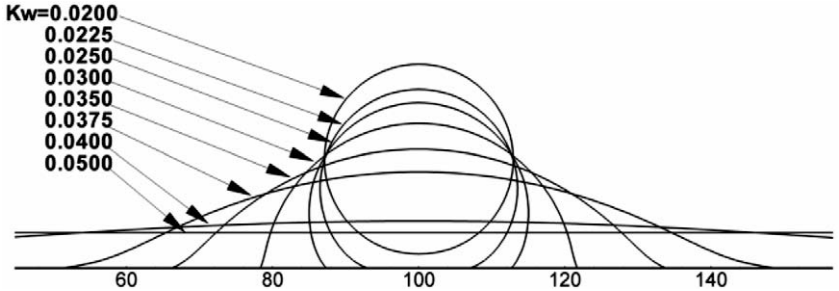

Fig. 9. Interfaces of droplet on wall with different wettabilities, $k_bT = 0.55$.

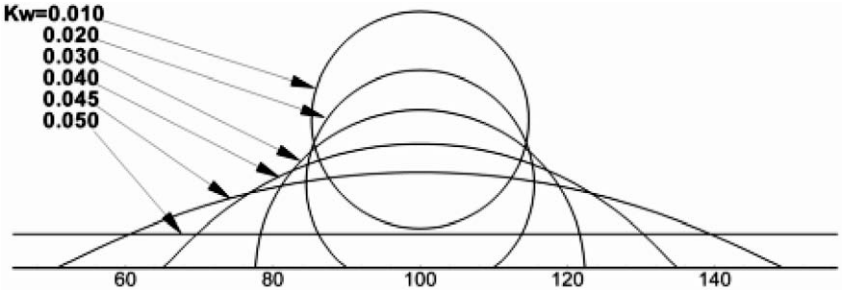

Fig. 11. Interfaces of droplet on wall with different wettabilities, $k_bT = 0.53$.

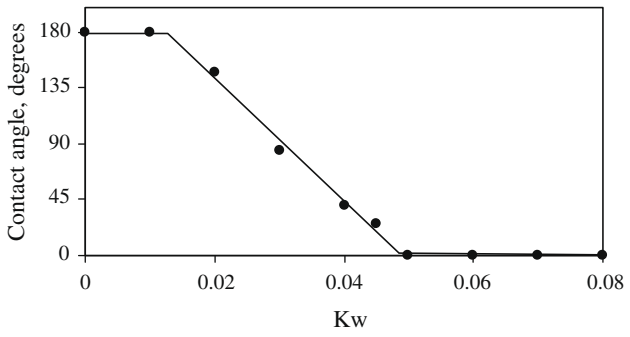

Fig. 12. Relation between contact angle and K_W, $k_bT = 0.53$; solid point is LBM simulations and solid line is their linear correlation.

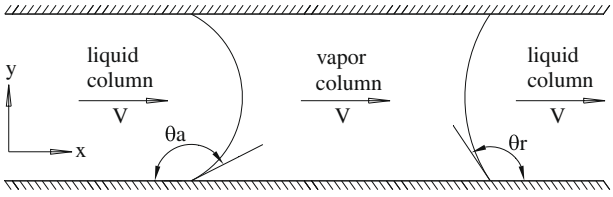

Fig. 13. A schematic of moving contact lines in channel flow: V is the interface velocity, θ_a and θ_r are advancing and receding contact angles, respectively.

cous, and inertia forces are represented through Reynolds number Re, capillary number Ca, and Weber number We:

$$\mathrm{Re} = \frac{2H_C V n_L}{\mu_L} \tag{36}$$

$$Ca = \frac{\mu_L V}{\gamma} \tag{37}$$

$$We = \mathrm{Re} \cdot Ca = \frac{2H_C n_L V^2}{\gamma} \tag{38}$$

where n_L and μ_L are liquid density and viscosity of the fluid, γ is the surface tension, and H_C is the height of the channel. As indicated by Eq. (38), the ratio of the Weber number to the capillary number defines the Reynolds number of the flow. Therefore, in the following presentation, we only display the capillary and Weber numbers.

The present simulations are performed with the collision relaxation time $\tau = 1.0$ at the temperature $k_bT = 0.53$. The surface tension of the fluid at this temperature is $\gamma = 0.023$ (Li and Tafti, 2007) and the kinematic viscosity is $v = 0.166667$ (based on Eq. (14)). The simulated channel is 1000 long and 35 wide, enclosing an initially rectangular vapor plug inside with the rest of the channel filled with the liquid. A periodic boundary condition is imposed at the inlet and outlet of the channel and the no-slip boundary condition is imposed on the two channel walls. The simulations start with zero velocity assigned over the whole domain. To provide a motive force, a constant body force $\mathbf{F}_o(\mathbf{x}) = f\mathbf{i}_\mathbf{x}$ is applied in the axial direction, where f is the magnitude of the body force. Different Reynolds numbers or Weber numbers are realized through applying different f.

We perform the simulations with 18 different f values, starting from 0.0 to 0.00091271 in an increment of 5.36888E−05. For each case, the LBM iterations are performed until 20,000 time steps. The recorded results show that the flows reach stationary states at around 2300–3000 time steps at which the moving interface shapes do not change. Fig. 14 shows the time evolution of axial locations of the two moving interfaces at $f = 0.000322133$. The axial locations of the two interfaces in the channel are displayed at two transverse locations each, one at the channel center and one on the top wall, resulting in four lines. Each of the four lines appears linear and parallel to each other, indicating that both the advancing and receding interfaces move at the same speed. The slopes of the four lines have the value 0.0259 which defines the speed V of the moving interfaces. With the speed V defined, both capillary number and Weber number are then computed, yielding $Ca = 1.008$ and $We = 10.961$.

Our simulation matrix is listed in Table 2, covering the range $Ca = 0$–3.883 and $We = 0$–162.748. The stationary results presented below are taken nominally at 20,000 time steps except when the vapor plug is crossing the inlet or outlet at this time step.

Fig. 15 displays the stationary interface contour lines (at the average fluid density) of the different driving forces. For clarity, only half of the simulations are shown in the figure, starting from $f = 0$ with a uniform increment of $\Delta f = 0.000107$. Fig. 15a and b displays the advancing and receding interfaces, respectively. When the diving force is zero, the two interfaces are at the equilibrium state and give the equilibrium contact angle $\theta_e = 78.1^\circ$. With the increase in driving force, interface speed, capillary number, and Weber number all increase as shown in Table 2. Meanwhile, both interfaces become distorted in the flow direction. When the driving force increases to the maximum, the vapor plug becomes severely

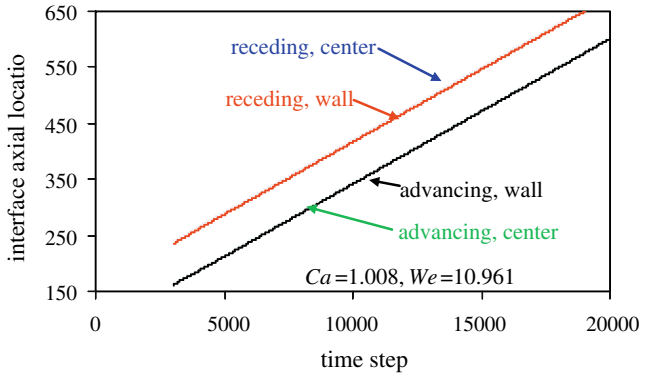

Fig. 14. Moving interface locations versus time, $Ca = 1.008$, and $We = 10.961$.

Table 2
Moving contact line simulation summary: body force f, interface velocity V, capillary number Ca, Weber number We, advancing angle θ_a, and receding contact angle θ_r.

Number	f	V	Ca	We	θ_a	θ_r
1	0	0.000	0.000	0.000	78.09	78.09
2	5.36888E−05	0.004	0.160	0.275	79.20	77.07
3	0.000107378	0.008	0.323	1.126	80.88	76.20
4	0.000161066	0.013	0.486	2.553	81.93	75.01
5	0.000214755	0.017	0.657	4.667	82.80	74.17
6	0.000268444	0.021	0.829	7.413	84.00	72.23
7	0.000322133	0.026	1.008	10.961	85.08	71.54
8	0.000375822	0.031	1.194	15.400	86.30	70.91
9	0.00042951	0.036	1.389	20.825	87.44	68.48
10	0.000483199	0.041	1.587	27.200	88.65	67.78
11	0.000536888	0.046	1.797	34.877	90.00	65.32
12	0.000590577	0.052	2.015	43.844	91.37	64.67
13	0.000644266	0.058	2.241	54.212	92.59	61.78
14	0.000697954	0.064	2.478	66.303	94.33	59.72
15	0.000751643	0.071	2.743	81.214	96.65	57.90
16	0.000805332	0.084	3.252	114.200	98.60	53.51
17	0.000859021	0.091	3.556	136.504	100.84	51.85
18	0.00091271	0.100	3.883	162.748	102.26	49.43

elongated, as shown in Fig. 15b. It is expected that the liquid droplet would pinch off from the wall and the vapor bubble would be broken with a further increase of the driving force.

In the literature, contact angle is computed either from the local coordinates of an interface near the solid wall or based on an equivalent circular approximation to the interface. In fact, as the capillary number increases, the interface shape deviates considerably from a circular shape. For the results shown in Fig. 15, these two procedures to approximate contact angles can lead to a difference up to 10° even at an intermediate capillary numbers. For this reason, all contact angles are computed based on the local coordinates of an interface near the wall. Table 2 includes the computed advancing and receding contact angles.

Table 2 shows that the advancing contact angles get larger and larger with an increase of capillary number or Weber number. Meanwhile, the receding contact angles become smaller and smaller. To validate our simulations in detail, a comparison is made with three existing typical theories of moving contact lines. Among the three theories, one is the widely used hydrodynamic theory due to Cox (1986) and one is the molecular kinetic theory by Blake

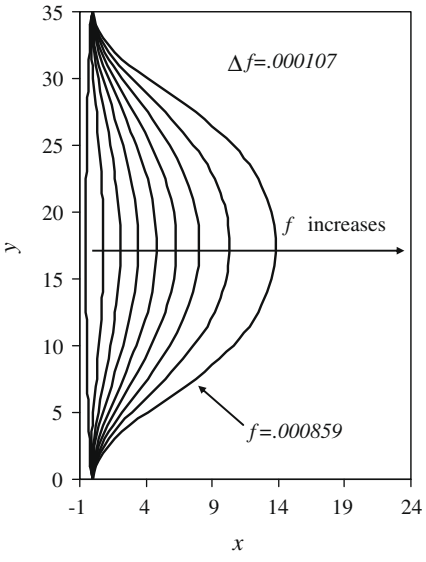

(a) Advancing Interfaces

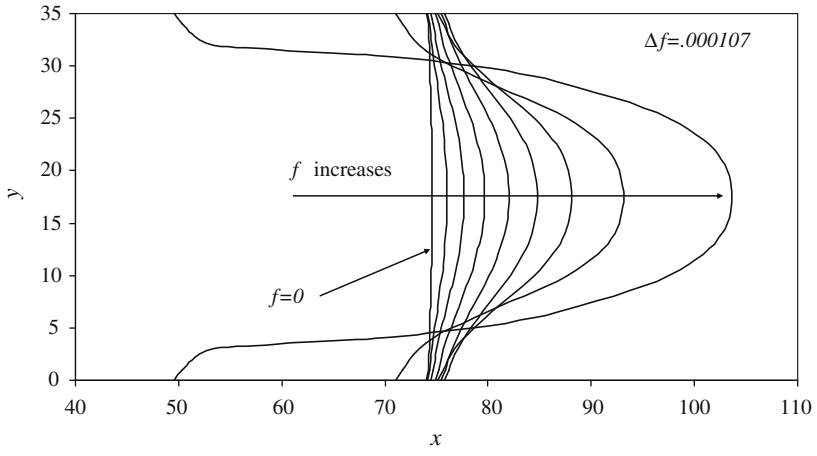

(b) Receding Interfaces

Fig. 15. Interface shapes for different driving forces, starting from $f = 0$ (the equilibrium case) with a uniform step increase of the body force ($\Delta f = 0.000107$). (a) Advancing interfaces; and (b) receding interfaces.

(1993). The third theory is the linear scaling law between cos θ and *Ca*.

4.4.2. Comparison with Cox theory

The hydrodynamic theory for moving contact line by Cox (1986) is based on a matching asymptotic expansion for low capillary numbers. The leading order expression of Cox theory gives the relation between the moving contact angle θ and the capillary number *Ca* as:

$$g(\theta) - g(\theta_e) = Ca\ln(\varepsilon_c^{-1}) + O(Ca) \tag{39}$$

where $g(\theta)$ is a function of dynamic contact angle θ, and defined as

$$g(\theta) = \int_0^{\theta} [f(\varphi)]^{-1}\, d\varphi \tag{40}$$

with

$$\begin{aligned} f(\varphi) = {} & 2\sin\varphi\Big\{q^2(\varphi^2 - \sin^2\varphi) + 2q[\varphi(\pi-\varphi) + \sin^2\varphi] \\ & + [(\pi-\varphi)^2 - \sin^2\varphi]\Big\} / \Big\{q(\varphi^2 - \sin^2\varphi)[(\pi-\varphi) + \sin\varphi\cos\varphi] \\ & + [(\pi-\varphi)^2 - \sin^2\varphi](\varphi - \sin\varphi\cos\varphi)\Big\} \end{aligned} \tag{41}$$

where q is the fluid density ratio of vapor to liquid; ε is the ratio of the microscopic slip length to the macroscopic characteristic length. According to Cox (1986), the microscopic slip length ε is not uniquely determined. For the current study, we use the approximation proposed by Sheng and Zhou (1992): $\varepsilon_c = l_d/k_s Ca$, where l_d is the wall roughness and k_s is a slipping-model dependent constant. As a result, Eq. (39) becomes

$$g(\theta) - g(\theta_e) = Ca\ln(k_s/l_d) + Ca\ln Ca \tag{42}$$

To solve the nonlinear equation (42), first, we numerically compute the integration of Eq. (40) for a series of different θ. For the current study, we compute the integration at $\theta = i\Delta\theta$, $i = 0, 1, 2, \ldots, 900$ and $\Delta\theta = 0.2^o$, with the fluid density ratio $q = 0.3014$. The numerical integration results are tabulated for $g(\theta)$ versus θ. For a given value of $g(\theta)$, we can find the related value of θ through an interpolation from the table. To solve Eq. (42) of Cox theory, we first find that $g(\theta_e) = 12.7191$ for the equilibrium contact angle $\theta_e = 78.1^o$ from the tabulated values. Then, we use the two constants $\ln(k_s/l_d) = 1.9$ and 2.5, separately. With each constant, we calculate the value of $g(\theta)$ for every *Ca* based on Eq. (42). With the value of $g(\theta)$ found for each *Ca*, we then find the moving contact angle θ through an interpolation from the tabulated function. Fig. 16 plots the results based on both our LBM simulations and Cox theory for the variation of the moving contact angles with Capillary numbers. The comparisons in Fig. 16 show that our LBM results are close to Cox theory with both constants, $\ln(k_s/l_d) = 1.9$ and 2.5. The variation in advancing angle with Capillary number is captured to within 10–15% by the LBM results.

4.4.3. Comparison with Blake theory

Blake's theory for moving contact line (Blake, 1993) is a kinetic model considering molecular adsorption/desorption near a moving contact line. The adsorbed molecules of a receding fluid are considered being replaced by the molecules of an advancing fluid at the moving contact line. The frequency of the molecular displacement is determined by the displacement frequency at equilibrium κ_w^0, the free-energy of the initial and activated thermodynamic states, and the adsorption sites per unit area m. The wetting velocity V is the result of the adsorption frequency times the average distance between two adjacent adsorption sites λ_b. Blake (1993) recognized that the driving force on a moving contact line is the out-of-balance interfacial tension force due to the difference between the moving contact angle θ and the equilibrium one θ_e. As a result, the wetting velocity V is related to the moving contact angle θ as

$$V = \alpha\sinh[\beta_b(\cos\theta_e - \cos\theta)] \tag{43}$$

where α and β are two constants, having the following forms:

$$\alpha = 2\kappa_w^0\lambda_b \tag{44}$$

$$\beta_b = \frac{\gamma}{2m_b k_b T} \tag{45}$$

The parameters κ_w^0, λ_b, and m_b are the model fitting constants, which are generally unknown and are obtained from experiments for a specific fluid and solid wall (Blake, 1993). Fig. 17 shows the comparison between the current LBM results and Blake theory, where the solid line represents the result of Blake theory with $\alpha = 0.23$ and $\beta_b = 1.0$ and the hollow circles represent the LBM results. The positive velocities are the results of the advancing interfaces while the negative velocities are those for the receding interfaces. These results show that the current LBM can also simulate Blake theory very well.

4.4.4. Comparison with the linear law of cos θ versus ca

The linear law of cos θ versus *Ca* is expressed as

$$\cos\theta_e - \cos\theta = \text{constant} \cdot Ca \tag{46}$$

The linear law has been obtained analytically by different researchers based on different points of view. The earlier work by Cherry and Holmes (1969) can directly lead to such an equation, as pointed out by Blake (1993). Joanny and Robbins (1990) found

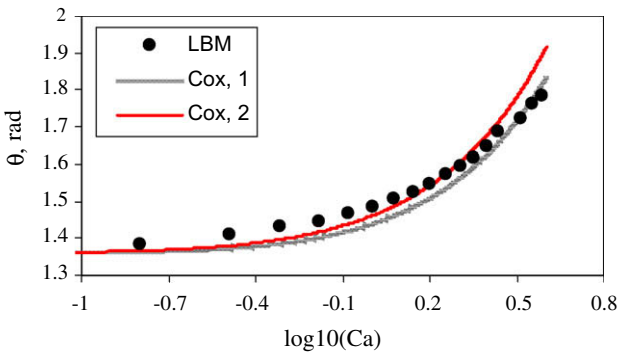

Fig. 16. Comparison between the current LBM and Cox theory for both $\ln(k_s/l_d) = 1.9$ (Cox, 1) and 2.5 (Cox, 2).

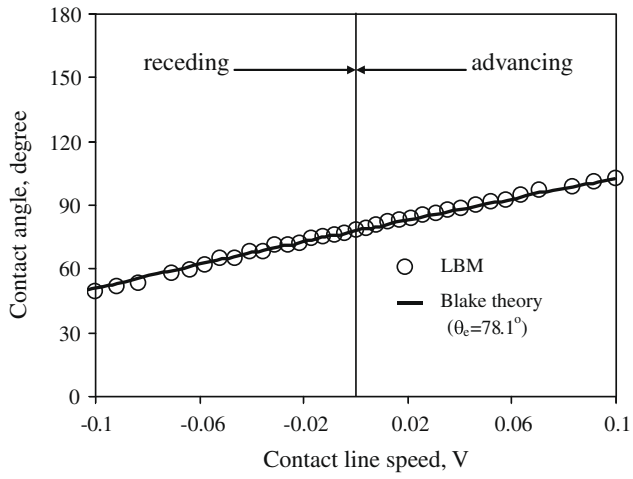

Fig. 17. Comparison between the current LBM and Blake theory, $\theta_e = 78.1^o$, with $\alpha = 0.23$ for both and $\beta_b = 1.0$.

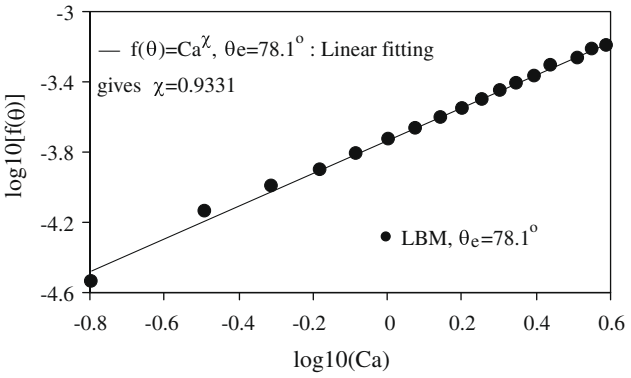

Fig. 18. D2Q9 LBM results of moving contact angle function $f(\theta)$ versus Ca, $f(\theta) = \cos\theta_e - \cos\theta$.

the same form of the equation holds under the condition of a smooth solid surface. De Gennes et al. (2004) obtain Eq. (46) from two points of view for moving contact line: a mechanical model of viscous dissipation and a molecular kinetic model of absorption/desorption. It is noted that in the different approaches to the linear law, the proportionality constant in the equation is defined differently but has the same physical meaning: The constant is equivalent to a friction coefficient. It should also be mentioned that Blake theory itself can reduce to the form of Eq. (46) when $\beta_b(\cos\theta_e - \cos\theta) \ll 1$.

To compare our results with the linear law, we plot our LBM data in Fig. 18 on a log–log scales, where the solid points represents LBM and the solid line is a linear correlation of the LBM. The slope of the linear correlation gives 0.9331 which is close to the theoretical value of unity as shown in Eq. (46).

5. Summary and conclusions

The mean-field free-energy formulation for liquid–vapor flows is implemented on a D2Q9 lattice configuration. It is shown that the extensively used common bounceback condition in the literature leads to an unphysical velocity at the wall in the presence of surface forces. The magnitude of the unphysical velocity is shown proportional to the local forces such as those arising from fluid–fluid attraction, fluid–solid attraction, and other surface forces. Based on Zou and He (1997), a new velocity-boundary condition to deal with the fluid–wall interaction is proposed, which eliminates the unphysical velocities. In addition, by imposing mass conservation, the new velocity-boundary condition has been further refined to improve the accuracy. The current model is shown to have the capability of successfully simulating static and dynamic liquid–vapor interfacial flows, with and without solid walls. The model shows very good agreement with the Laplace law of capillarity, and capillary wave dynamics. In particular, the current D2Q9 model with the new boundary condition successfully simulates the challenging moving contact line problem and shows good agreement with three well established theories of contact line dynamics.

References

Allen, M.P., Tildesley, D.J., 1987. Computer Simulations of Fluids. Clarendon Press, Oxford.

Anderson, D.M., McFadden, G.B., Wheeler, A.A., 1998. Diffuse-interface methods in fluid mechanics. Annu. Rev. Fluid Mech. 30, 139–165.

Antanovskii, A., 1995. A phase field model of capillarity. Phys. Fluids 7, 747–753.

Barrat, J.-L., Bocquet, L., 1999. Large slip effect at a nonwetting fluid–solid interface. Phys. Rev. Lett. 82, 4671–4674.

Blake, T.D., 1993. Dynamic contact angles and wetting kinetics. In: Berg, J.C. (Ed.), Wettability. Marcel Dekker, New York.

Briant, A.J., Papatzacos, P., Yeomans, J.M., 2002. Lattice Boltzmann simulations of contact line motion in a liquid–gas system. Philos. Trans. R. Soc. Lond. A 360, 485–495.

Briant, A.J., Wagner, A.J., Yeomans, J.M., 2004. Lattice Boltzmann simulations of contact line motion. I. Liquid–gas systems. Phys. Rev. E 69, 031602.

Cahn, J.W., Hilliard, J.E., 1958. Free energy of a nonuniform system. I. Interfacial free energy. J. Chem. Phys. 28, 258–267.

Chen, S., Chen, H.D., Martinez, D., Mathhaeus, W.H., 1991. Lattice Boltzmann model for simulation of magnetohydrodynamics. Phys. Rev. Lett. 67, 3776–3779.

Chen, H., Chen, S., Mathhaeus, W.H., 1992. Recovery of the Navier–Stokes equations using a lattice-gas Boltzmann method. Phys. Rev. A 45, R5339–R5342.

Cherry, B.W., Homes, C.M., 1969. Kinetics of wetting of surfaces by polymers. J. Colloid Interface Sci. 29, 174–176.

Cox, R.G., 1986. The dynamics of the spreading of liquids on a solid surface. Part I. Viscous flow. J. Fluid Mech. 168, 169–194.

De Gennes, P.G., 1985. Wetting: statics and dynamics. Rev. Mod. Phys. 57, 827–863.

De Gennes, P.-G., Brochard-Wyart, F., Quéré, D., 2004. Capillarity and Wetting Phenomena, Drop, Bubbles, Pearls, Waves. Springer, Berlin. Translated by Axel, Reisinger.

De Ruijter, M.J., Blake, T.D., Coninck, J.D., 1999. Dynamic wetting studied by molecular modeling simulations of droplet spreading. Langmuir 15, 7836–7847.

Dussan, E.B., 1979. On the spreading of liquids on solid surfaces: static and dynamic contact lines. Annu. Rev. Fluid Mech. 11, 371–400.

Gunstensen, A.K., Rothman, D.H., Zaleski, S., 1991. Lattice Boltzmann model of immiscible fluids. Phys. Rev. A 43, 4320–4327.

He, X., Doolen, G.D., 2002. Thermodynamic foundations of kinetic theory and lattice Boltzmann models for multiphase flows. J. Stat. Phys. 107, 309–328.

He, X., Shan, X., Doolen, G.D., 1998. Discrete Boltzmann equation model for nonideal gases. Phys. Rev. E 57, R13–R16.

Hirt, C.W., Nichols, B.D., 1981. Volume of fluid (VOF) methods for the dynamics of free boundaries. J. Comput. Phys. 39, 201–225.

Jacqmin, D., 1999. Calculation of two-phase Navier–Stokes flows using phase-field modeling. J. Comput. Phys. 155, 96–127.

Jacqmin, D., 2000. Contact line dynamics of a diffuse fluid interface. J. Fluid Mech. 402, 57–88.

Jamet, D., Lebaigue, O., Coutris, N., Delhaye, J.M., 2001. The second gradient method for the direct numerical simulation of liquid–vapor flows with phase change. J. Comput. Phys. 169, 624–651.

Jasnow, D., Vinals, J., 1996. Coarse-grained description of thermo-capillary flow. Phys. Fluids 8, 660–669.

Joanny, J.F., Robbins, M.O., 1990. Motion of a contact line on a heterogeneous surface. J. Chem. Phys. 92, 3206–3212.

Lamb, H., 1945. Hydrodynamics, sixth ed. Dover, New York (Chapter 9).

Landau, L.D., Lifshitz, E.M., 1987. Fluid Mechanics, second ed. Pergamon Press, New York (Chapter 7).

Lee, T., Lin, C.-L., 2005. Rarefaction and compressibility effects of the lattice-Boltzmann-equation method in a gas microchannel. Phys. Rev. E 71, 046706.

Li, S.-M., Tafti, D.K., 2006. Contact line dynamics in liquid–vapor flows using lattice Boltzmann method. In: ASME Paper FEDSM2006-98022, Proceedings of FEDSM2006 006 ASME Joint US–European Fluids Engineering Summer Meeting, July 17–20, Miami, FL.

Li, S.-M., Tafti, D.K., 2007. A mean-field pressure formulation for liquid–vapor flow. ASME Trans. J. Fluids Eng. 129, 894–901.

Luo, L., 1998. Unified theory of lattice Boltzmann models for nonideal gases. Phys. Rev. Lett. 81, 1618–1621.

Oron, A., Bankoff, S.G., Davis, S.H., 1997. Long-scale evolution of thin liquid films. Rev. Mod. Phys. 69, 931–980.

Osher, S., Sethian, J.A., 1988. Fronts propagating with curvature-dependent speed: algorithms based on Hamilton–Jacobi formulations. J. Comput. Phys. 79, 12–49.

Qian, Y.H., D'Humieres, D., Lallemand, P., 1992. Lattice BGK models for Navier–Stokes equation. Europhys. Lett. 17, 479–484.

Qian, T., Wang, X.-P., Sheng, P., 2003. Molecular scale contact line hydrodynamics of immiscible flows. Phys. Rev. E 68, 016306.

Qian, T., Wang, X.-P., Sheng, P., 2004. Power-law slip profile of the moving contact line in two-phase immiscible flows. Phys. Rev. Lett. 93, 094501.

Rowlinson, J.S., 1979. Translation of J.D. van der Waals. The thermodynamic theory of capillarity under the hypothesis of a continuous variation of density. J. Stat. Phys. 20, 197–244.

Rowlinson, J.S., Widow, B., 1982. Molecular Theory of Capillarity. Clarendon press, Oxford.

Sethian, J.A., 1996. Level Set Methods. Cambridge University Press, Cambridge.

Shan, X., Chen, H., 1993. Lattice Boltzmann model for simulating flows with multiple phases and components. Phys. Rev. E 47, 1815–1819.

Shan, X., Chen, H., 1994. Simulation of nonideal gases and liquid–gas phase transitions by the lattice Boltzmann equation. Phys. Rev. E 49, 2941–2948.

Sheng, P., Zhou, M., 1992. Immiscible-fluid displacement: contact-line dynamics and the velocity-dependent capillary pressure. Phys. Rev. A 45, 5694–5708.

Shkhmurzaev, Y.D., 1997. Moving contact lines in liquid/liquid/solid systems. J. Fluid Mech. 334, 211–249.

Sullivan, D.E., 1981. Surface tension and contact angle of a liquid–solid interface. J. Chem. Phys. 74, 2604–2615.

Swift, M.R., Orlandini, E., Osborn, W.R., Yeomans, J.M., 1996. Lattice Boltzmann simulations of liquid–gas and binary-fluid systems. Phys. Rev. E 54, 5041–5052.

Swift, M.R., Osborn, W.R., Yeomans, J.M., 1995. Lattice Boltzmann simulation of nonideal fluids. Phys. Rev. Lett. 75, 830–833.

Unverdi, S.O., Tryggvason, T., 1992a. Computations of multi-fluid flows. Phys. D 60, 70–83.
Unverdi, S.O., Tryggvason, T., 1992b. A front-tracking method for viscous, incompressible, multi-fluid flows. J. Comput. Phys. 100, 25–37.
Van Giessen, A.E., Bukman, D.J., Widom, B., 1997. Contact angles of liquid drops on low-energy solid surfaces. J. Colloid Interface Sci. 192, 257–265.
Van Giessen, A.E., Blokhuis, E.M., Bukman, D.J., 1998. Mean field curvature correlation to the surface tension. J. Chem. Phys. 108, 1148–1156.
van Kampen, N.G., 1964. Condensation of a classical gas with long-range attraction. Phys. Rev. 135, A362–369.
Yang, Z.L., Dinh, T.N., Nourgaliev, R.R., Sehgal, B.R., 2001. Numerical investigation of bubble growth and detachment by the lattice-Boltzmann method. Int. J. Heat Mass Transfer 44, 195–206.
Zhang, J., Li, B., Kwok, D.Y., 2004. Mean-field free-energy approach to the lattice Boltzmann method for liquid–vapor and solid–fluid interfaces. Phys. Rev. E 69, 032602-1–032602-4.
Zou, Q., He, X., 1997. On pressure and velocity boundary conditions for the lattice Boltzmann BGK model. Phys. Fluids 9, 1591–1597.